frontiers | Frontiers in Energy Research

TYPE Original Research
PUBLISHED 19 February 2024
DOI 10.3389/fenrg.2024.1325865

OPEN ACCESS

EDITED BY
Kumaran Kadirgama,
Universiti Malaysia Pahang, Malaysia

REVIEWED BY
Hind Barghash,
German University of Technology in Oman, Oman
Sree Lakshmi Gundebommu,
CVR College of Engineering, India

*CORRESPONDENCE
Praveen Kumar Balachandran,
praveenbala038@gmail.com

RECEIVED 22 October 2023
ACCEPTED 30 January 2024
PUBLISHED 19 February 2024

CITATION
Srilakshmi K, Rao GS, Balachandran PK and Senjyu T (2024), Green energy-sourced AI-controlled multilevel UPQC parameter selection using football game optimization. *Front. Energy Res.* 12:1325865. doi: 10.3389/fenrg.2024.1325865

Green energy-sourced AI-controlled multilevel UPQC parameter selection using football game optimization

Koganti Srilakshmi[1], Gummadi Srinivasa Rao[2], Praveen Kumar Balachandran[3]* and Tomonobu Senjyu[4]

[1]Department of Electrical and Electronics Engineering, Sreenidhi Institute of Science and Technology, Hyderabad, India, [2]Department of Electrical and Electronic Engineering, Velagapudi Ramakrishna Siddhartha Engineering College, Vijayawada, India, [3]Department of Electrical and Electronics Engineering, Vardhaman College of Engineering, Hyderabad, India, [4]Faculty of Engineering, University of the Ryukyus, Nishihara, Japan

The power quality (PQ) has been significantly affected by the integration of intermittent non-conventional sources (NCS) into the local distribution system in addition to the adoption of power electronic technologies to regulate non-linear loads. This article combines the H-bridge cascade five-level unified power quality conditioner (5L-UPQC) with the wind power generation system (WPGS), solar photovoltaic power generation system (SPVGS), and battery storage system (BSS) as an effective approach to address PQ problems. The utilization of the Levenberg–Marquardt backpropagation (LMBP)-trained Artificial neural network controller (ANNC) in the UPQC is recommended for generating appropriate reference signals for the converters. This eliminates the requirement for conventional complex conversions, such as abc, dq0, and αβ. Moreover, the artificial neuro-fuzzy interface system (ANFIS) is recommended for achieving a DC-link balance. Football game optimization (FBGO) is utilized to determine the optimal shunt and series filter characteristics. The major objectives of the proposed system are to reduce the current waveform irregularities, resulting in a decrease in the total harmonic distortion (THD), an enhancement in the power factor (PF), the mitigation of supply voltage imbalances and disturbances, and the maintenance of a steady direct-current link capacitor voltage (DLCV), despite the variations in the load, solar irradiation, and wind velocity. The efficiency of the suggested strategy is assessed using four case studies that involve different loads, variable wind velocities, and source voltage balancing conditions. Based on the simulation studies and obtained results, the suggested method significantly decreases the THD to values of 2.91%, 3.63%, 3.75%, and 3.50%. Additionally, it achieves a power factor of unity, which is considerably lower compared to other multilevel schemes that use the traditional symmetrical reference frame (SRF) and instantaneous reactive power (pq) methods. This design has been executed using the MATLAB/Simulink program.

KEYWORDS

total harmonic distortion, shunt active power filter, series-active power filter, unified power quality conditioner, football game optimization

1 Introduction

In recent years, integrating renewable energy systems, like solar and wind, into the distribution network has been encouraged to reduce the stress on converters and ratings. The output of a traditional square-wave inverter is a square wave with a significant amount of harmonics. This necessitates the use of filters to tailor the output and create a sinusoidal shape. When employing traditional square-wave inverters, the cost and size of the filter rise, which becomes a significant disadvantage. An admirable property of multilevel inverters is that they produce leveled output. Compared to traditional square-wave inverters, leveled output requires smaller filters.

1.1 Motivation for the research work

Lately, there has been a growing emphasis on the role of unified power quality conditioner (UPQC) in distributed power generation systems. The integration of UPQC with a non-conventional source (NCS) has become increasingly crucial compared to the traditional grid-connected voltage source converter (VSC). This approach offers several benefits, including the maintenance of a stable direct-current link capacitor voltage (DLCV) amidst load fluctuations, improvement in the power quality (PQ) on the grid, ensuring the safety of sensitive loads against disturbances from the grid side, and enhancing the fault ride-through capability of the converter during transient events. Notably, UPQC combined with NCS systems is particularly well-suited for three-phase three-wire distribution systems. One key aspect of UPQC is the generation of reference signals. In the existing literature, the methods for generating reference signals for the series and shunt compensators of UPQC have primarily relied on complex techniques, such as the dq and instantaneous reactive power (pq) theory. However, in an effort to circumvent these complexities, electrical engineers are increasingly turning to artificial intelligence controllers.

1.2 Literature review

The solar-integrated UPQC was developed to address PQ issues efficiently. In order to obtain the most power and maintain the DLCV balance, a unique fuzzy-based proportional integral controller (PIC) was created for the maximum power tracking technique (Yang et al., 2019). In addition, an innovative hybrid-enhanced method for the shunt active power filter (SHAPF) connected with the artificial neural network (ANN) technology was introduced to minimize current waveform flaws and boost PQ in the distribution network (Ganesan and Srinath, 2019). The best tuning of a fractional-order proportional integral controller for reactive power and harmonic compensation under balanced and unbalanced loading conditions was then used to construct the particle swarm optimization (PSO) and gray-wolf optimization (GWO)-based optimal SHAPF, which was then tested experimentally (Mishra et al., 2020). However, using hysteresis and pulse-width modulation (PWM) approaches, the effectiveness of wind systems associated with UPQC was investigated under various loads and problematic conditions (DheyaaIed and Goksu, 2022). Additionally, using the technique of impedance matching, the flow of power in UPQC was examined on a three-phase system under various working conditions (Zhao et al., 2021).

Additionally, the power flow analysis of UPQC was investigated on a three-phase distribution grid under various operating situations using the method of impedance matching (Yap et al., 2017). Moreover, the fuzzy-based hybrid technique was adopted to achieve the maximum out of the photovoltaics (PVs). However, to reduce complexity, the ANN was considered for UPQC reference signal generation to solve PQ issues (Srilakshmi et al., 2023). To reduce the current total harmonic distortion (THD), the intelligent fuzzy-tuned PIC was created for the hybrid shunt active and passive filters. By utilizing Clarke's transformation, the performance study was carried out for various loads (Lin and Simachew, 2022). Solar-supplied UPQC was also introduced to lower the THD of the supply current at voltage variations, like sag and swell, by utilizing the ANN. Additionally, under various load conditions, the developed approach was contrasted with symmetrical reference frame (SRF) and pq methods (Okech et al., 2022). An evolutionary PSO and GWO algorithm was proposed to select optimal K_p and K_i values of the PIC of the SHAPF to minimize the THD and manage reactive power, respectively (Mishra et al., 2022). However, to regulate DLCV and to handle power, the feed-forward ANN has been suggested for PV/wind-associated UPQC (Chandrasekaran et al., 2021).

To lower THD in the grid current waveform, the H-bridge inverter-based single phase SHAPF with a modified predictive current control approach was introduced (Belqasem et al., 2022). Furthermore, the microgrid-connected multilevel D-STATCOM was developed to eliminate voltage and current distortions effectively (Sarker et al., 2020). Furthermore, a comprehensive study was carried out on various phase synchronization techniques that were used to control the working of the SHAPF (Yap et al., 2019). The novel technique was introduced for the UPQC to improve the power quality to regulate energy transfer between sources and loads (Szromba, 2020).

For the AC–DC microgrid system, intelligent hybrid controllers, such as fuzzy-PIC and fuzzy PID controllers, were developed to increase the PQ and stabilize the voltage in the presence of D-STATCOM (NafehHeikalEl-Sehiemy and Salem, 2022). However, the GWO was suggested to optimize the gain values of PIC-based UPQC to reduce the THD for both linear and non-linear loads (Marcel et al., 2023). Hysteresis current control was used for pulse generation, stabilizing the DLCV for SHAPF to effectively deal with PQ issues. Additionally, linear and non-linear loads were considered to study the performance (Imam et al., 2020). Biogeography-based optimization (BBO) was selected to obtain optimal gain values of the PIC and for fast action in fault identification with higher accuracy with the motive of stabilizing DLCV fluctuations (Sayed et al., 2021).

The hybrid fuzzy-ANN control technique has been adopted for UPQC to minimize the current THD and voltage fluctuations and improve the network usage (Renduchintala et al., 2021). The improved bat and moth–flame metaheuristic optimization methods were hybridized to solve the PQ issues by the optimal selection of the gain values of PIC (Rajesh et al., 2021). The fuzzy logic controller (FLC) was developed for the series-active power filter (SeAF) of the distribution network to minimize the current- and voltage-related PQ problems (Pazhanimuthu and Ramesh, 2018).

The predator–prey firefly algorithm was selected for the optimal selection of the gain values of the PIC adapted to the

TABLE 1 Literature survey.

Reference/ year	Control		PQ issues				Loads	
[No]/year	Reference signal generation	Controller	THD	DLCV balancing	Supply voltage sag and swell	Supply voltage disturbance	Non-linear sensitive load	Unbalanced load
Mishra et al. (2020)/ 2020	pq theory	FOPID	✓				✓	✓
DheyaaIed and Goksu. (2022)/2022	SRF	PIC	✓					
Srilakshmi et al. (2023)/2023	ANN	ANN	✓	✓	✓	✓	✓	✓
Lin and Simachew. (2022)/2022	SRF	Fuzzy-PI	✓	✓			✓	
Chandrasekaran et al. (2021)/2021	ANN	ANN	✓		✓		✓	✓
Sayed et al. (2021)/ 2021	SRF	PI-BBO	✓		✓		✓	✓
Rajesh et al. (2021)/ 2021	SRF	ANFIS	✓				✓	✓
Pazhanimuthu and Ramesh. (2018)/ 2018	pq	Fuzzy	✓		✓		✓	
Sahithullah et al. (2019)/2019	SRF	PPFFA	✓				✓	✓
(Sakthivel et al., 2015)/2019	SRF	PI-ACO	✓				✓	✓
Sudheer and Kota. (2017)/2017	ANN	ANN	✓	✓	✓		✓	✓
Ramadevi et al. (2023)/2023	SRF	FF-ANN	✓	✓	✓	✓	✓	✓
Proposed 5L-UPVBES	**ANFIS**	**ANFIS**	✓	✓	✓	✓	✓	✓

The bold values shows the proposed method (to highlight the best result).

SHAPF to reduce the THD and to enhance the power factor (PF) (Sahithullah et al., 2019). Soccer match optimization for the optimal selection of weights for the ANN controller was suggested for PV/battery-associated UPQC to solve PQ issues (Koganti et al., 2022). The ant colony optimization (ACO) algorithm was chosen for selecting the K_p and K_i values of the PIC for the SHAPF to reduce the THD under several loading conditions (Sakthivel et al., 2015). An adaptive novel hysteresis band with the FLC was suggested to the PV-powered nine-level VSC of UPQC to receive fluctuation-free signals (Hassan et al., 2022). Next, the soccer match algorithmic approach was suggested for the appropriate choice of PIC gain values for UPQC to successfully handle both voltage fluctuations and current distortions (Srilakshmi et al., 2022).

For UPQC, the hybrid control strategy combining the FLC and ANN features was suggested as a way to lessen the flaws in the grid's voltage and current waveforms while still maintaining DLCV for dynamic loads (KogantiKrishna and Reddy Salkuti, 2022). The ANN-based method was suggested for five-level UPQC to control the PQ problems (Sudheer and Kota, 2017). The firefly-based optimization algorithm was used to train the ANNC, which was developed for the shunt VSC for the PV/battery UPQC to reduce the mean-square error (MSE) and minimize the THD (Ramadevi et al., 2023). The self-tuning filter-based method was developed for UPQC integrated with renewable sources to address PQ issues (Mansoor et al., 2023). The Levenberg–Marquardt backpropagation (LMBP)-trained ANN controller was adopted for UPQC to mitigate the current- and voltage-related PQ problems efficiently (Zhou et al., 2006).

Moreover, a special improved UPQC with several objectives and variables that can be optimized using the BHO and PSO techniques to alter the PIC variables has been designed to decrease the system THD (Khosravi et al., 2023). Furthermore, a suggestion was made to use power-compensating approaches to connect the AC/DC microgrid to the grid in order to lower the harmonic amplitudes. This entails maximizing the gain coefficients in specific filter compensation apparatuses. The PIC's optimized coefficients were linked to the cost

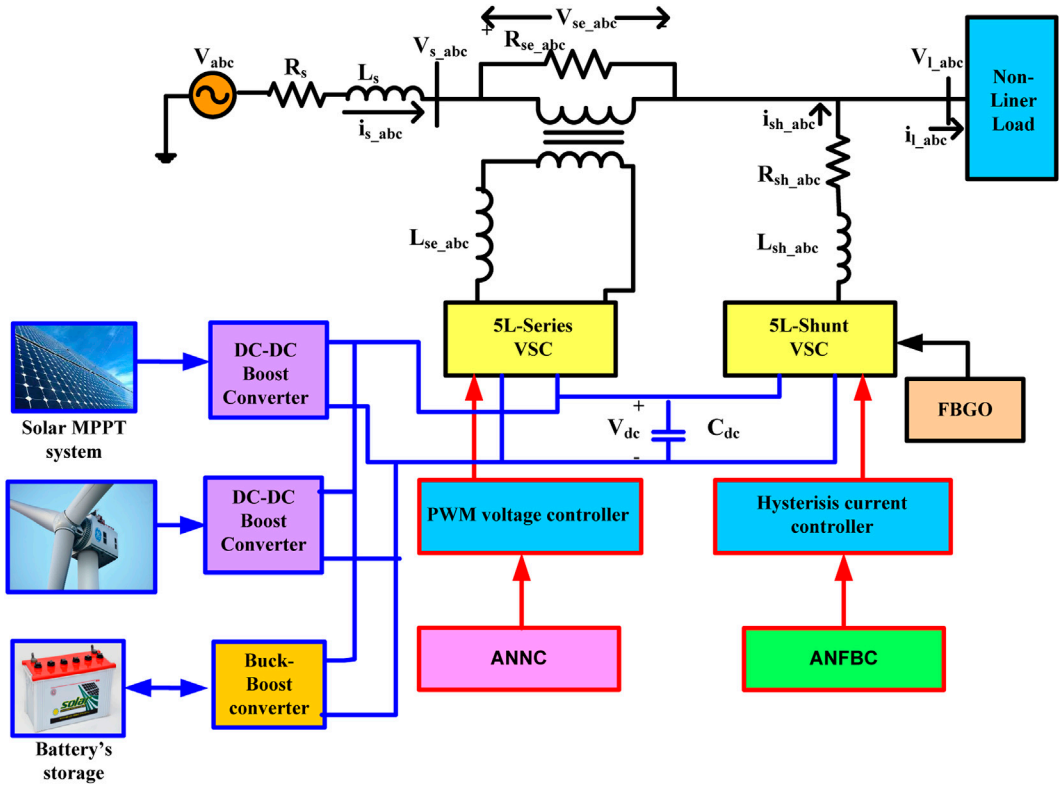

FIGURE 1
Proposed 5L-MUPQC configuration.

functions that took into account the inaccuracy of the controller, voltage harmonics, and current harmonics (Khosravi et al., 2021).

1.3 Key contribution

The literature listed in Table 1 makes it abundantly evident that the majority of the works mostly concentrated on different controllers using the pre-existing traditional control methods for UPQC that included complicated Park's and Clarke's transformations. In addition to an artificial neuro-fuzzy interface system (ANFIS) controller for DC-link balancing, this publication develops ANN-based reference signal generation for the PV/battery-coupled DC-link UPQC.

The novelty of this manuscript is highlighted in the steps below:

- ➢ Introducing the Levenberg–Marquardt-trained ANNC for generating effective reference signals in order to eliminate the necessity of complex abc–dq0–αβ0 conversions, i.e., SRF and pq theories in UPQC.
- ➢ The optimal selection of the H-bridge cascade 5L-UPQC shunt and series filter parameters for effectively reducing the imperfections in the current waveforms effectively using football game optimization (FBGO).
- ➢ Proposing the hybrid ANFIS controller to maintain a constant DLCV.
- ➢ Incorporating solar power with storage systems of the DC link of 5L-UPQC to reduce the stress and burden on the VSC, which supports and meets the load demand and maintains a constant DLCV during load variations.
- ➢ The objective of the proposed system is to diminish the source current THD and eliminate the grid voltage side troubles, like disturbance, swell, and sag.
- ➢ Additionally, the suggested ANFIS for 5L-UPQC in association with the PV, wind, and battery storage system (BSS) (5L-MUPQC) is examined on four test cases for several types of loads, solar irradiation, and wind velocity to show its superior performance.

This paper is structured as follows: Section 2 shows the modeling of 5L-UPQC, Section 3 explains the proposed control scheme, Section 4 demonstrates the results and discussion, and Section 5 concludes the manuscript.

2 Modelling of the developed 5L-MUPQC

Figure 1 shows the proposed 5L-UPQC configuration, which connects the PVs and batteries to the DC link of UPQC. Combining series and shunt VSCs creates UPQC. By supplying the appropriate compensation voltage via the injecting transformer and the inductor, the SHAPF seeks to resolve grid-side voltage-related issues. The SHAPF is similarly connected to the grid via the interface inductance.

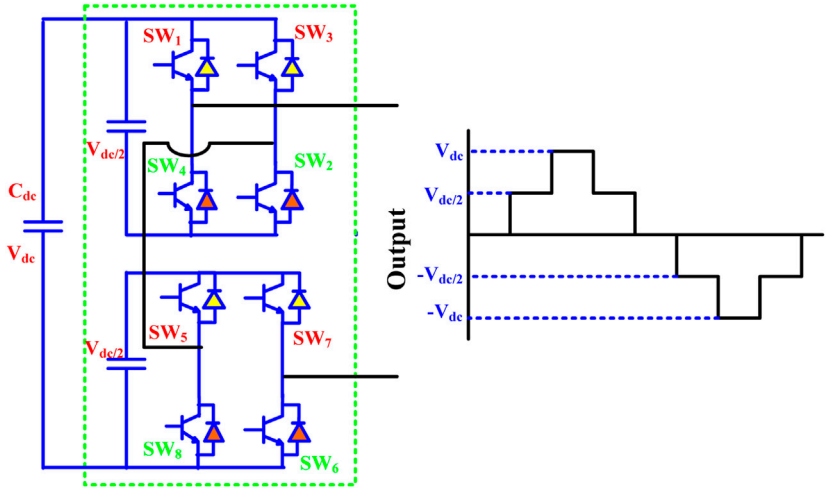

FIGURE 2
Single-phase 5L-cascade H-bridge UPQC with the output.

TABLE 2 On/off of switches considered for 5L-cascaded H-bridge UPQC.

Output voltage	SW1	SW2	SW3	SW4	SW5	SW6	SW7	SW8
V_{dc}	1	1	0	0	1	1	0	0
$V_{dc/2}$	1	1	0	0	1	0	1	0
0	1	0	1	0	1	0	1	0
$-V_{dc/2}$	0	0	1	1	1	0	1	0
V_{dc}	0	0	1	1	0	0	1	1

Note*: 0 = off; 1 = on.

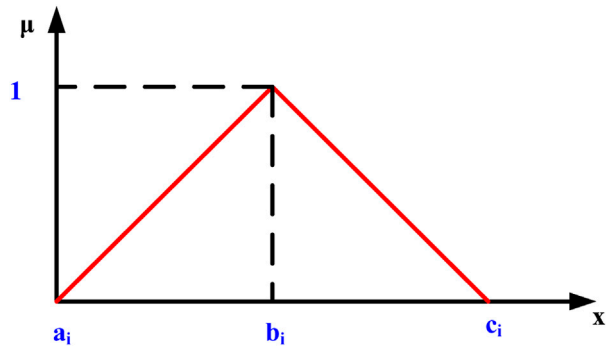

FIGURE 3
Triangular membership function (MSF).

By injecting a sufficient compensating current, the SHAPF seeks to decrease the current waveform harmonics and maintain the DLCV constant with a minimal settling time.

One of the best structures is the multilevel inverter cascaded H-bridge topology, which requires no clamping tools or components. Although the cascaded H-bridge topology's layout is straightforward, more DC sources are needed to power each single H-bridge cell. Two H-bridge cells are cascaded into a five-level H-bridge structure, and every single H-bridge cell is powered by a DC source. Figure 2 displays a multilevel inverter five-level cascaded H-bridge arrangement; it also displays the cascaded H-bridge's 5L voltage output in the phase. The five-level output is produced by sequentially triggering power switches as the whole DC-link voltage is divided across two H-bridge cells. Figure 2 shows the power switches used for five-level cascaded H-bridge, and its switching order is given in Table 2.

2.1 Selection of C_{dc}

The value of C_{dc} can be calculated by Eq. 1:

$$C_{dc} = \frac{\pi^* i_{sh}}{\sqrt{3}\omega V_{cr,pp}}. \quad (1)$$

V_{dc}^{ref} is chosen within the suggested system's permissible rating range.

2.2 Selection of L_{sh} and L_{se}

The shunt VSC is linked to the network through an inductor (L_{sh}), given by Eq. 2, which relies on the switching frequency, ripple current, and DLCV; it is given as follows:

TABLE 3 DC-link power distribution.

Mode of operation	Action taken
Mode-1: When no *SPG* and *WPG*	BES only will provide power to P_{DC}
Mode-2: When *SPG* and *WPG* = P_{DC}	Solar PV and wind will supply power P_{DC}
Mode-3: When *SPG* and *WPG* <P_{DC}	Difference sum of the power will be provided by the battery until it reaches $SOCB_{\min}$
Mode-4: When *SPG* and *WPG* >P_{DC}	Excessive solar power is used to charge the battery system until it reaches $SOCB_{\max}$

TABLE 4 NCS ratings.

Device	Parameter/source	Value chosen
WS	Power at output	3 MW
	Velocity of wind	11 m/s
	Pitch integral gain controller K_i	5
	Pitch proportional gain controller K_p	25
	Max rate of change of PA	45 deg
	Pitch angle	25 deg./second
Li-ion BSS	Rated-capacity of the battery	450 Ah
	Maximum battery capacity	550 Ah
	Voltage	650 V
	Full-charged voltage	757 V
SPVG	Output power	214.92 W
	Open circuit voltage	48.3 V
	Short-circuit current	5.8 A
	Voltage/current under max power	39.80 V/5.40 A

$$L_{sh} = \frac{\sqrt{3}\, m V_{dc}}{12\, a_f\, f_{sh}\, I_{cr,pp}}, \tag{2}$$

assuming m is 1, a_f is 1.5, and f_{sh} is 10 kHz. Similarly, L_{se} is given by Eqs 3, 4

$$K_{se} = \frac{V_{L-L}}{\sqrt{3}\, V_{se}}, \tag{3}$$

$$L_{se} = \frac{\sqrt{3}\, m V_{dc} K_{se}}{12\, a_f\, f_{se}\, I_{cr,pp}}. \tag{4}$$

Assuming f_{se} as 10 kHz, the series inductance depends on the ripple current.

2.3 External support for 5L-MUPQC at the DC link

The solar/battery-fed DC link is proposed for the diode-clamped 5L-UPQC. It consists of a hybrid solar and battery energy system to regulate the DLCV at changing loads. External support can reduce the converter ratings and stress by lowering the utility's demands. The equation for the power demand of the suggested technique is given in Eq. 5:

$$P_{PV} + P_W + P_{BSS} - P_{Load} = 0. \tag{5}$$

The PV model used in this work was selected from the Simulink library. To create the necessary quantity of voltage and current, the PV modules are connected in series to form a string. Some of these strings are then connected in parallel. Here, Eq. 6 describes the solar output. Figure 3 illustrates the PV cell properties for a fixed temperature and changing irradiance. The incremental conductance-based MPPT is adopted to extract the maximum output from the PV system (Srilakshmi et al., 2023):

$$P_{PV} = V_{PV} \times i_{PV}. \tag{6}$$

Moreover, the BSS aids in supporting the DLCV's stabilization. The cells are stacked in parallel or series in a battery to provide the necessary voltage and current. Since Li-ion batteries have benefits like slower discharge and inexpensive maintenance costs, this work chooses them from the Simulink library. The state of charge of the battery (*SOCOB*) (Koganti et al., 2022) is expressed in Eq. 7:

$$SOCOB = 80\left(1 + \int i_{BSS}\, dtQ\right). \tag{7}$$

The SPG will choose whether to charge or discharge the battery while adhering to the restrictions stated by Eq. 8. Figure 5 depicts the battery's drain. Table 3 displays the power division at DC's link capacitor, and Table 4 provides the ratings selected for PV, battery, and wind systems. Figure 4 shows the control mechanism for the solar, wind, and battery system fed to the DC link.

$$SOCOB_{\min} \le SOCOB \le SOCOB_{\max}. \tag{8}$$

The wind-generated AC voltage is rectified into the DC voltage, which is then boosted through a boost converter. A permanent magnet synchronous machine was considered in the present work. Wind power generation (KogantiKrishna and Reddy Salkuti, 2022) is given by Eqs 9–13:

$$P_m = 1/2\pi\, \rho\, C_p\, (\lambda, \beta)\, R^2\, V^3, \tag{9}$$

$$\lambda = \frac{\omega_m R}{v}, \tag{10}$$

$$\omega_m = \omega_t\, G_r, \tag{11}$$

$$C_p\, (\lambda, \beta) = 0.23\left(\frac{116}{\lambda_1} - 0.48\beta - 5\right)\exp^{\frac{-12.5}{\lambda_1}}, \tag{12}$$

$$\lambda_1 = \left(\frac{1}{\frac{1}{\lambda - 0.02\beta} - \frac{0.0035}{3\beta + 1}}\right). \tag{13}$$

3 Proposed control scheme

Generally, chances take place at the distribution side during dynamic load variations. For a brief period, the system must be restored to its

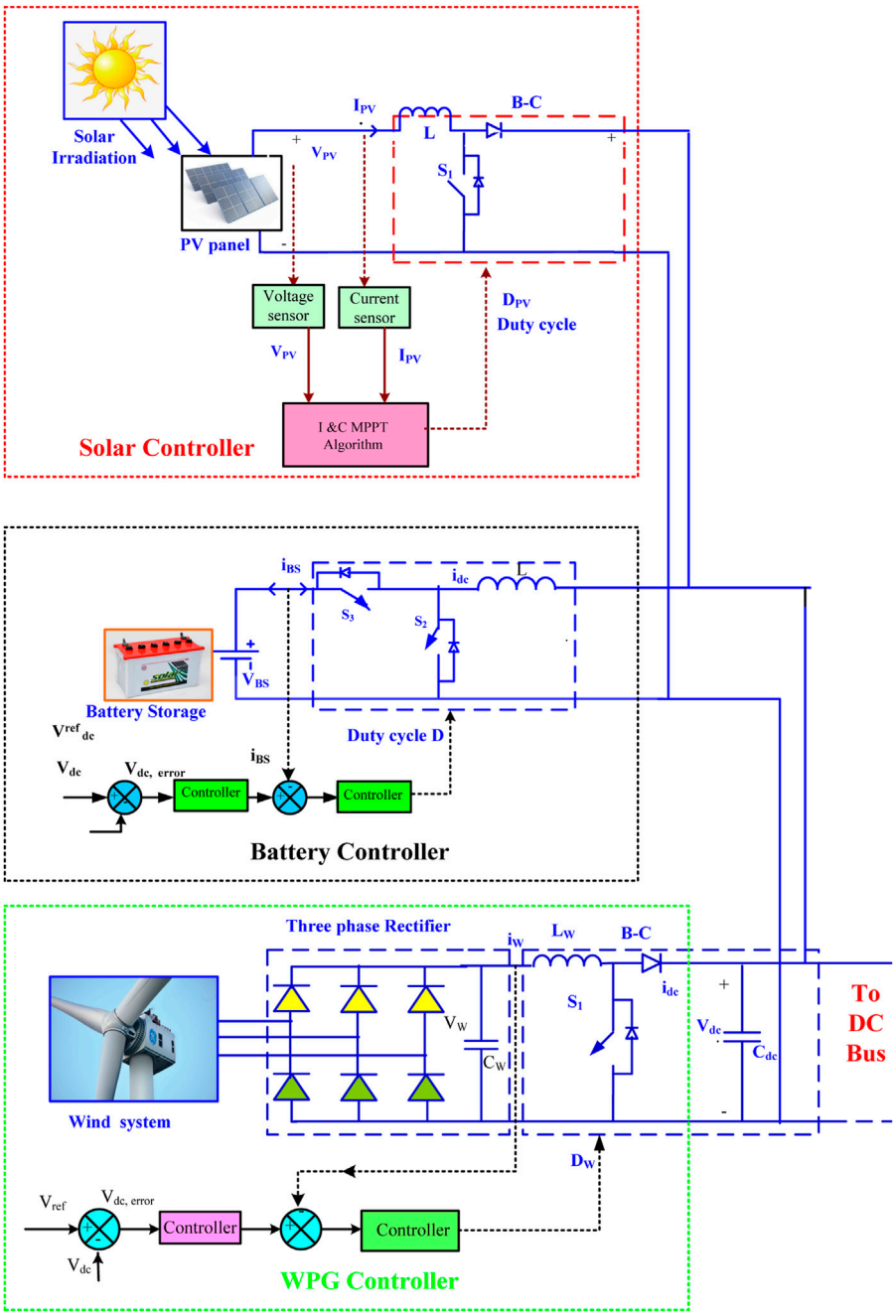

FIGURE 4
Control of photovoltaic (PV), wind, and battery systems with boost and buck–boost converters.

initial value in order to function normally. Here, using the recommended ANNC, the PWM hysteresis current control for the shunt VSC and gate pulses for the series VSC are produced by the PWM technique.

3.1 Shunt VSC

The major goal of the SHAPF is to manage the DLCV under faults and dynamic loading circumstances and to suppress current signal distortions by injecting the compensating current. The output layer (OL), input layer (IL), and hidden layer (HL) components of the ANN make up its structure, where the IL gathers data supplied as input and sends it to the HL. When linked between the IL and the HL, it is afterward multiplied by the appropriate weights on the connected links. Here, calculations are performed with a chosen bias on the HL, and the outcomes are gathered in the OL.

In this case, the LMBP-based ANN is chosen. To get the desired output, the weights of the link are adjusted during training by analyzing the mistake. For ANN training, where the performance function is the MSE, the LMBP training method is used. The LMBP algorithm updates the weights using the obtained derivatives, which has the advantages of rapid convergence and effective learning.

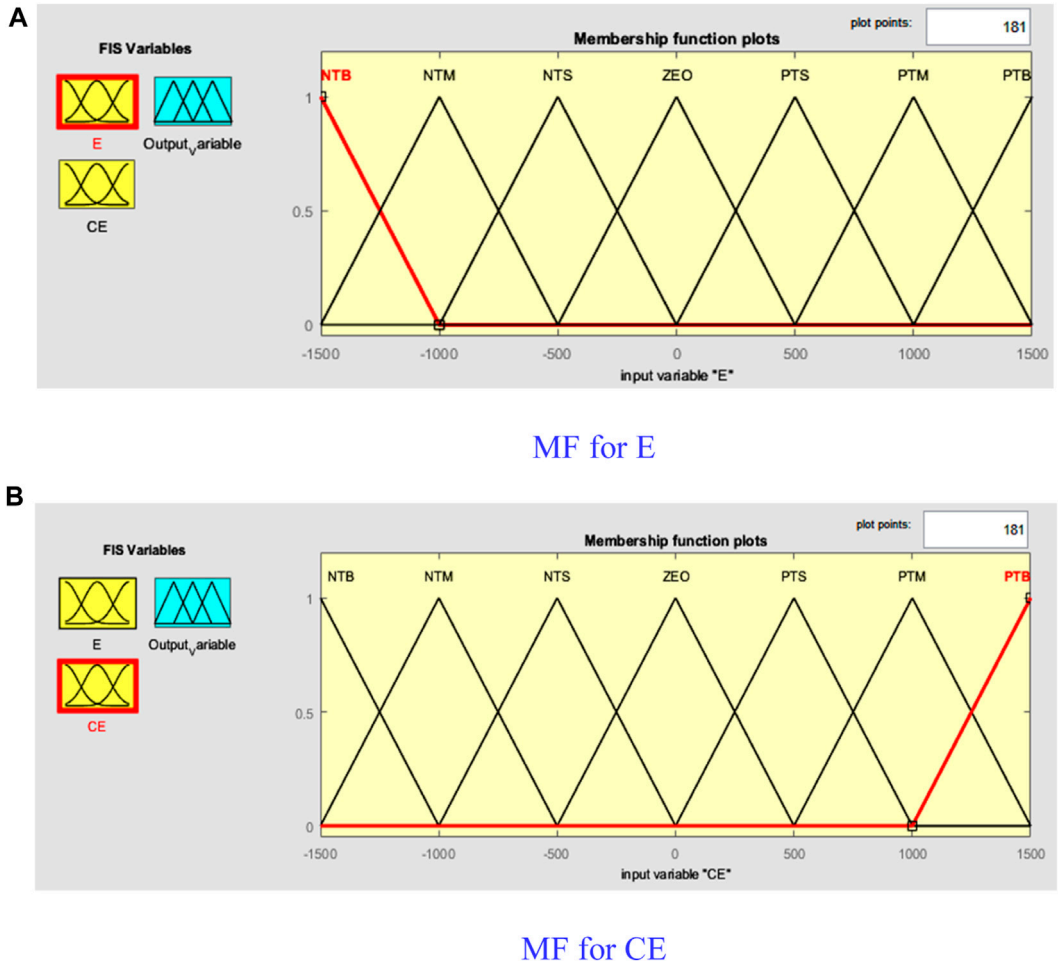

FIGURE 5
Fuzzy MSF for **(A)** E, **(B)** CE.

3.1.1 ANFIS

It is advised that the ANFIS keeps the DLCV constant. The proposed ANFIS combines fuzzy logic and ANN elements to create an intelligent hybrid controller. However, in order to keep the DLCV constant, the obtained DLCV—whose output, E, and CE are taken into consideration—is compared to the selected reference DLCV. As seen in Figure 5, the inputs given to the ANNC are first trained based on the Gaussian membership function (MSF) to yield the best results. The ANFIS is primarily composed of five layers: the first layer, called fuzzification, produces the fuzzy MSF, which is given by Eq. 14 and is depicted in Figure 5.

$$\begin{matrix} \mu_{Ai}(x), i = 1, 2. \\ \mu_{Bj}(y), j = 1, 2.' \end{matrix} \tag{14}$$

where $\mu_{Ai}\mu_{Bj}$ are the MSF outputs obtained from the first layer. The representation of the triangular MSF is exhibited by Eq. 15:

$$\mu_{Ai}(x) = \max\left(\min\left(\frac{x - a_i}{b_i - a_i}, \frac{c_i - x}{c_i - b_i}\right), 0\right), \tag{15}$$

where b_i is the fuzzy set i's point of greatest support and x_{max}–x_{min} (high and low bonds) is the range (world of discourse) of x. The inputs that are taken into consideration are the negative-big (NEB), negative-medium (NEM), zero (ZOE), positive-small (PES), positive-big (PEB), positive-medium (PEM), and negative-small (NES) input. MF's inputs are displayed in Figure 5. We can see the fuzzy rule base in Table 5.

TABLE 5 Lower and upper bounds of variables.

Decision variable	R_{sh} (Ω)	L_{sh} (mH)	R_{se} (Ω)	L_{se} (mH)
Lower	0	0.01	0	0.01
Upper	0.5	10	2	10

Furthermore, the AND operator is used in the second layer (where fuzzy rule weighting is carried out) to calculate the firing strength w_i by accounting for the MSF produced in the initial layer, the result of which is ascertained using Eq. 16:

$$w_k = \mu_{Ai}(x)^*\mu_{Bj}(y)i, j = 1, 2. \tag{16}$$

The third layer is where the values from the previous layer are normalized. Normalization is achieved at each node in this layer by computing the ratio, as given in Eq. 17, of the firing strength (true

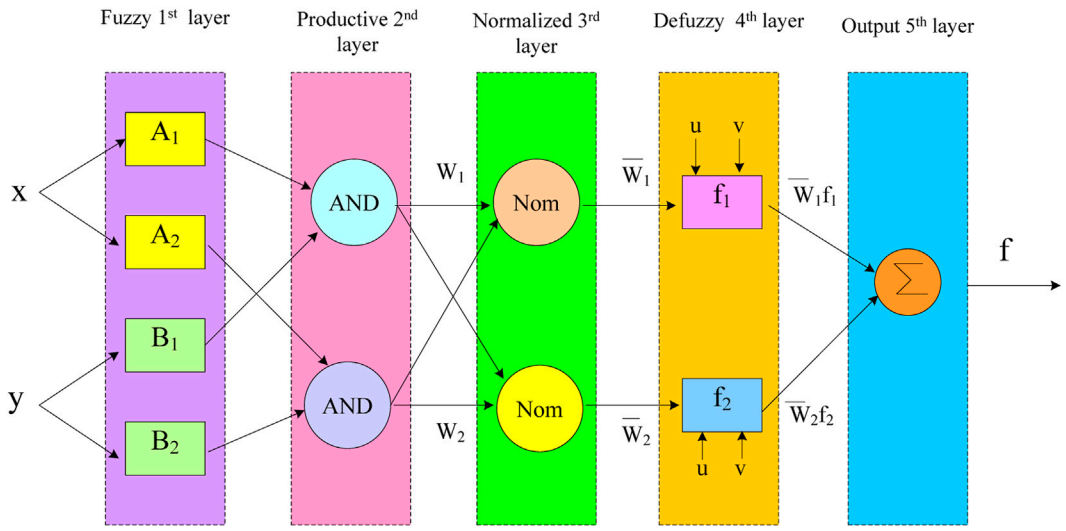

FIGURE 6
Structure of the artificial neuro-fuzzy interface system (ANFIS).

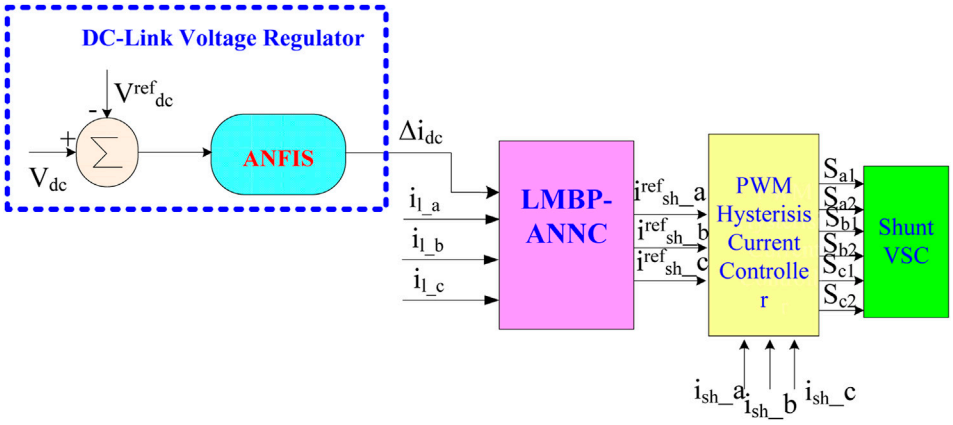

FIGURE 7
Control of the shunt converter.

values) of the kth rule to the sum of the firing strengths of all other rules:

$$\overline{w_k} = \frac{w_k}{w_1 + w_2} k = 1, 2. \tag{17}$$

The self-adaptive capability of the ANNC is executed through the application of the inference parameters (p_k, q_k, r_k) in the fourth layer, which produces an output as defined in Eq. 18:

$$\overline{w_i} f_i = \overline{w_i}(p_k u + q_k v + r_k). \tag{18}$$

As shown in Eq. 19, the inputs are finally combined in the fifth layer to provide the final required total output of the ANFIS. The suggested ANFIS's configuration and the MSF for inputs 1 and 2 are shown in Figure 6.

$$f = \sum_i \overline{w_i} f_i. \tag{19}$$

In this work, the ANFIS is trained to keep the DLCV stable and to generate reference current signals. However, for keeping the DLCV constant, the reference DLCV (V^{ref}_{dc}) is compared with the actual DLCV (V_{dc}); its error is chosen as input data, Δi_{dc}. Subsequently, the load currents (i_{l_abc}) and the DC loss component (Δi_{dc}) are regarded as the input, whereas the reference currents ($i^{ref}_{sh\_abc}$) are regarded as target data, as depicted in Figure 7. Figure 8 shows the selected neurons' structure.

3.2 Series VSC

The main function of the series filter is to reduce source voltage signal imperfections by injecting an appropriate compensating voltage to keep the load voltage constant. The suggested series VSC reference signal production strategy is shown in Figure 9, and the construction of an ANN with an HIL of 200 neurons is

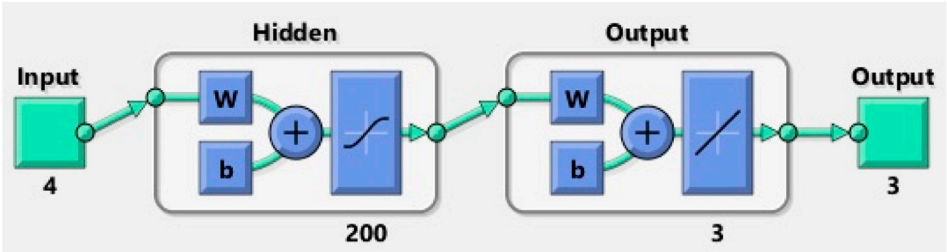

FIGURE 8
ANNC for referencing the current generation.

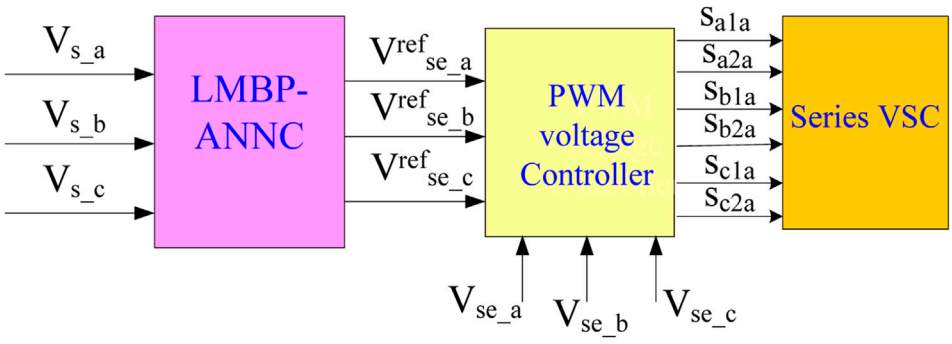

FIGURE 9
Series voltage source converter (VSC) controller.

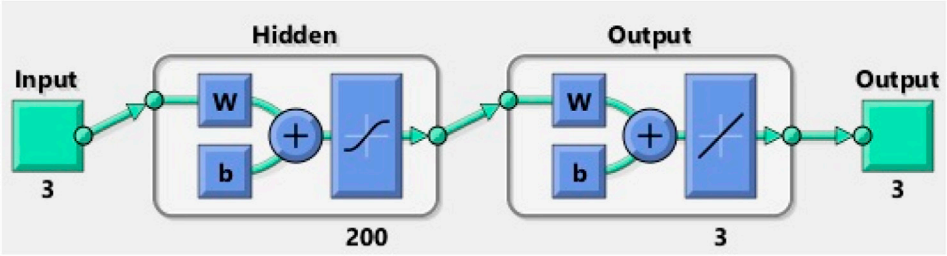

FIGURE 10
Structure of the ANNC for reference voltage generation.

shown in Figure 10. The supply voltages (V_{s_abc}) are regarded as data for the input to produce the reference voltage signals ($V^{ref}_{se\_abc}$), whereas the reference voltage is regarded as the goal data to the ANN. Moreover, the PWM produces pulses for a series converter.

4 FBGO-based shunt and series filter parameter selection

FBGO is a metaheuristic optimization algorithm that simulates the behaviors of football players. Within this framework, a team of players is established, and the position of each player corresponds to a solution point on the football field. The evaluation of each player's performance is based on the performance function (PEF), which is derived from the objective function (Eq. 26). The movements of these players, guided by a team coach, mimic the process of obtaining the ball and reaching a goal, involving two distinct phases: random walk and coaching. The proposed method is used to determine the optimal values of resistance and inductances of shunt and series filters (variables) with the goal of minimizing the THD. Each player is defined to denote the problem variables, as given in Eq. 20. The upper and lower bounds of variables are given in Table 5.

$$P_i = L_{sh}, L_{se}, R_{sh}, R_{se}, \tag{20}$$

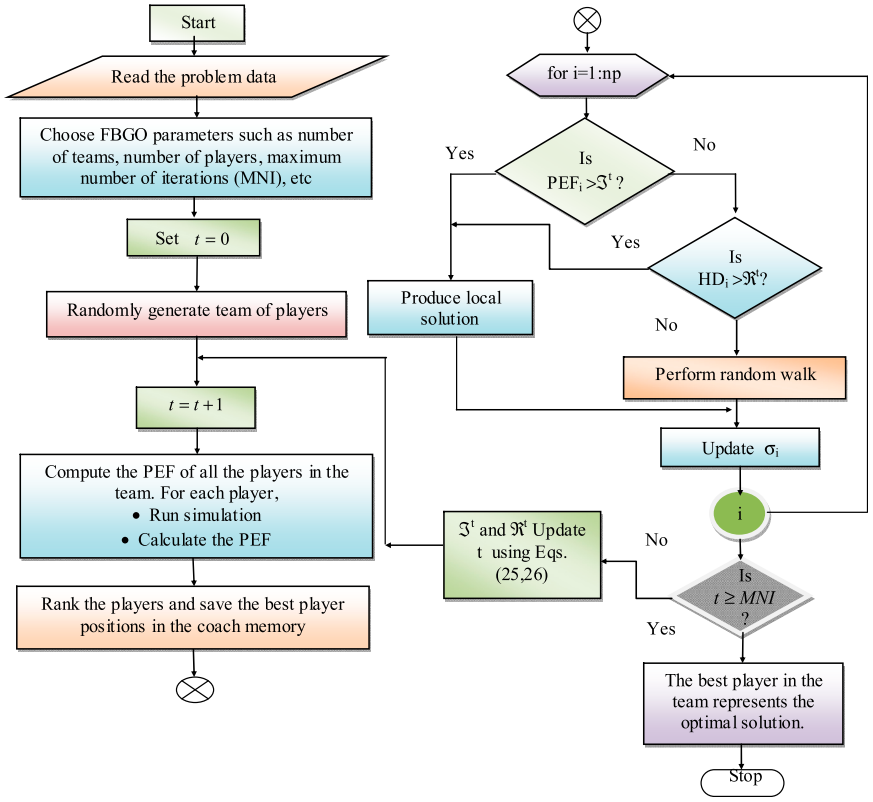

FIGURE 11
Flowchart of football game optimization (FBGO) for the proposed system.

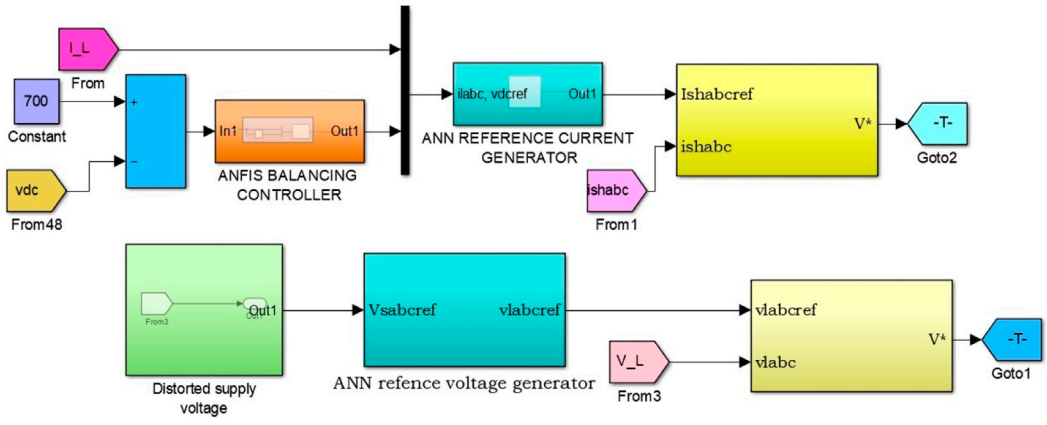

FIGURE 12
Simulink models of proposed M-UPQC with the ANFIS controller.

$$PEF = \frac{1}{1 + THD}. \tag{21}$$

The random player movements, under the supervision of a team coach, follow a two-step process to accomplish the tasks of retrieving the ball and reaching the goal, as detailed below.

4.1 Random walk

Individually, every player embarks on a random walk, aiming to locate a position closer to the ball with the aspiration of scoring a goal. During this phase, there are no specific instructions or guidance from the coach.

TABLE 6 5L-UPQC parameters with loads.

Grid supply	V_s, 415 V; f, 50 Hz; R_s, 0.1 Ω; and L_s, 0.15 mH
SHAPF	Hysteresis-controller band: 0.01
DC link	C_{dc}, 9400 μF; V_{dc}^{ref} = 700V
Loads	1. Balanced 3 Φ rectifier type load: L = 1 mH and R = 10Ω
	2. Balanced 3 Φ rectifier type load: L = 0.5 mH and R = 5Ω
	3. Balanced load: p = 1000 W and Q = 500 Var
	4. Unbalanced 3 Φ RL-type load: R1 and L1 = 10 Ω and 1.50 mH; R2 and L2 = 20 Ω and 3.5 mH; and R3 and L3 = 15 Ω and 2.5 mH

TABLE 7 Test cases studies considered for different loads.

Condition	Case 1	Case 2	Case 3	Case 4
Balanced V_S	✓	✓		
Unbalanced V_S			✓	✓
Steady-state voltage			✓	✓
Steady-state current			✓	✓
V_{Sag}	✓			
V_{Swell} and disturbance		✓		
Current during V_{Sag}, V_{Swell}, and disturbance	✓	✓		
Constant wind velocity of 11 m/s	✓			✓
Variable wind velocity		✓	✓	
Constant solar irradiation 1000 W/m^2	✓	✓		
Variable solar irradiation			✓	✓
Load 1	✓		✓	✓
Load 2		✓	✓	
Load 3	✓			
Load 4		✓		✓

$$P_i^t = P_i^{t-1} + \delta_i\sigma + \gamma\left(P_B^t - P_i^{t-1}\right). \tag{22}$$

σ_i is reduced for every iteration by $\sigma_i = \sigma_i\Theta$.

4.2 Coaching

The player heightens the pressure on their opponent by advancing as directed by the game coach, taking into account the hyper distance (HD) between players, which is determined by Eq. 23:

$$HD_i = \left\|P_i^{t-1} - P_{best}^{t-1}\right\|. \tag{23}$$

Players whose HD values exceed a certain threshold, denoted as "$\mathfrak{R}$", are directed to relocate themselves closer to the optimal nearby positions, $P_{near-best}^{t-1}$, by Eq. 24:

$$P_i^t = P_{near-best}^{t-1} + \sigma_i\delta. \tag{24}$$

The value of "$\mathfrak{R}$" is slowly reduced toward its designated minimum value ($\mathfrak{R}_{\min}$) through Eq. 25, and η resembles the constant.

$$\mathfrak{R}^t = \mathfrak{R}_{\min} + \eta\left(\mathfrak{R}^{t-1} - \mathfrak{R}_{\min}\right). \tag{25}$$

In the substitution plan, the team coach replaces ineffective players with better players to improve the chances of achieving a goal. Each proficient player, whose PEF exceeds the cost constraint value ($\mathfrak{F}$), is exchanged for a nearby skilled player, according to the coach's memory (CM), using Eq. 5. $\mathfrak{F}$ will gradually be reduced as the iteration moves, as defined by Eq. 26:

$$\mathfrak{F}^t = \mathfrak{F}_{\min} + \varepsilon\left(\mathfrak{F}^{t-1} - \mathfrak{F}_{\min}\right), \tag{26}$$

where ε indicates the succession constant. If the new player strays from the soccer field, they are returned to the field through the use of Eq. 24.

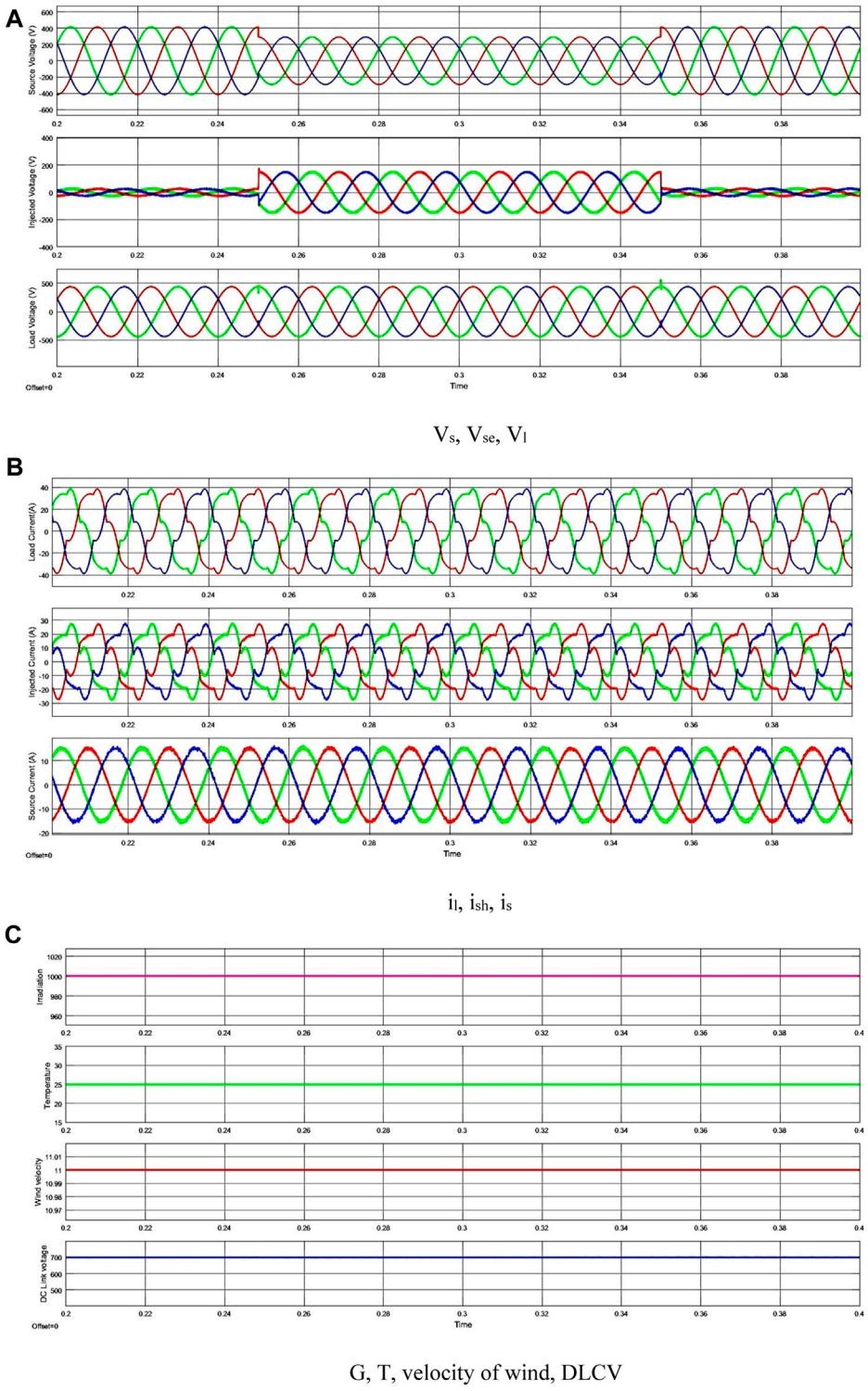

FIGURE 13
Waveforms for the first case study.

4.3 Solution process

A set of players is initially generated with random values, and their PEFs are calculated using Eq. 21. Following this, they are ranked based on their PEF. The HD between each player and the most efficient player is computed. Subsequently, the random walk and coaching steps are carried out using Eqs 22, 23, respectively. The entire cycle, encompassing the PEF evaluation, HD computation, and the execution of random walks and coaching, constitutes the iteration. This process is repeated until convergence is achieved. The player with

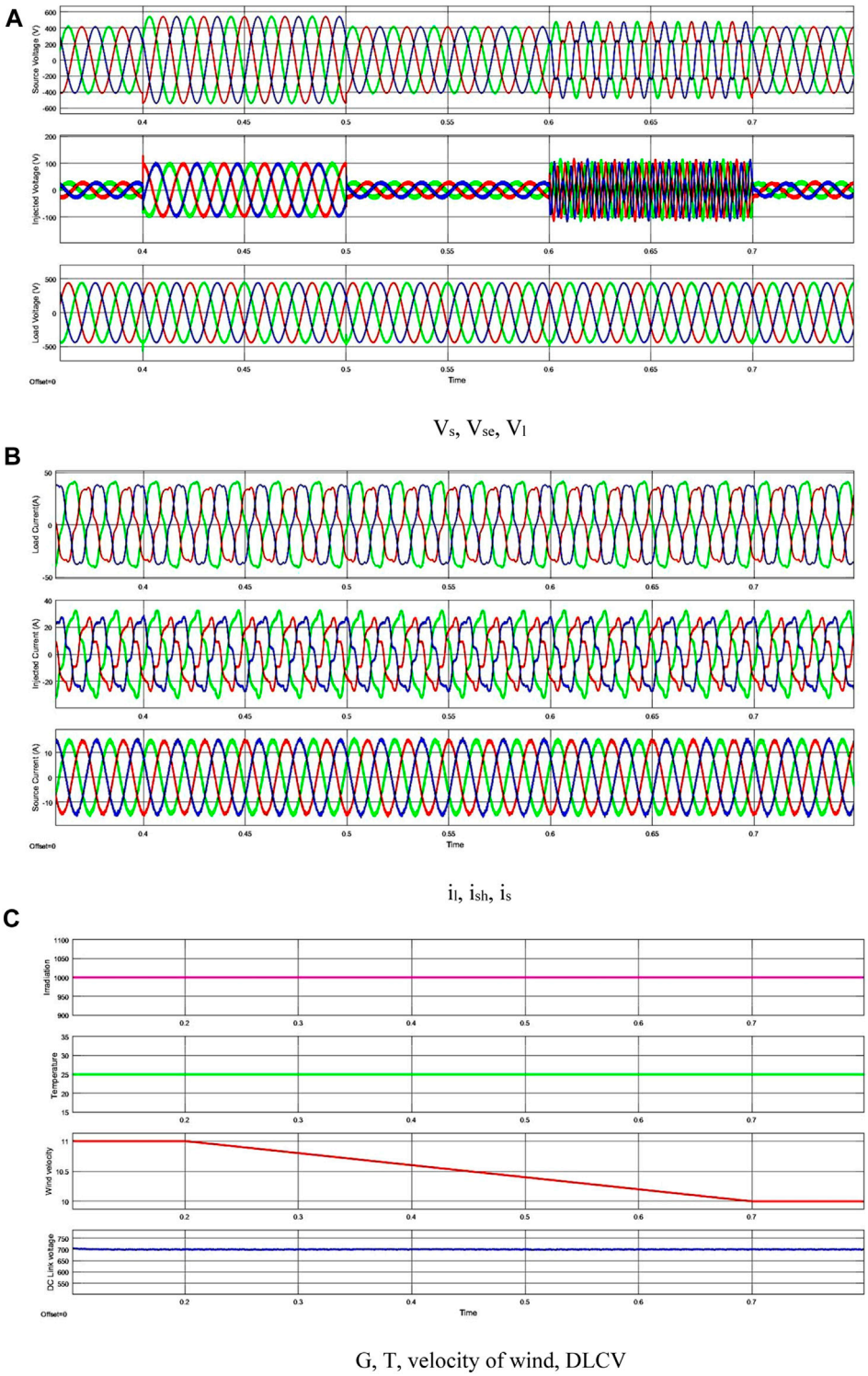

FIGURE 14
Waveforms for the second case study.

the highest PEF is identified as the optimal player once convergence is reached. Figure 11 gives the flowchart of the algorithm for the solution. FBGO has a higher efficiency with faster convergence; it is capable of solving multi-objective and complex engineering problems effectively. Moreover, it has its own limitations, like being a computational burden.

5 Results and discussions

Using MATLAB 2016a, the suggested M-UPQC with ANFBC was created. Figure 12 displays the suggested method's Simulink model. Table 6 also shows the system and the UPQC parameters

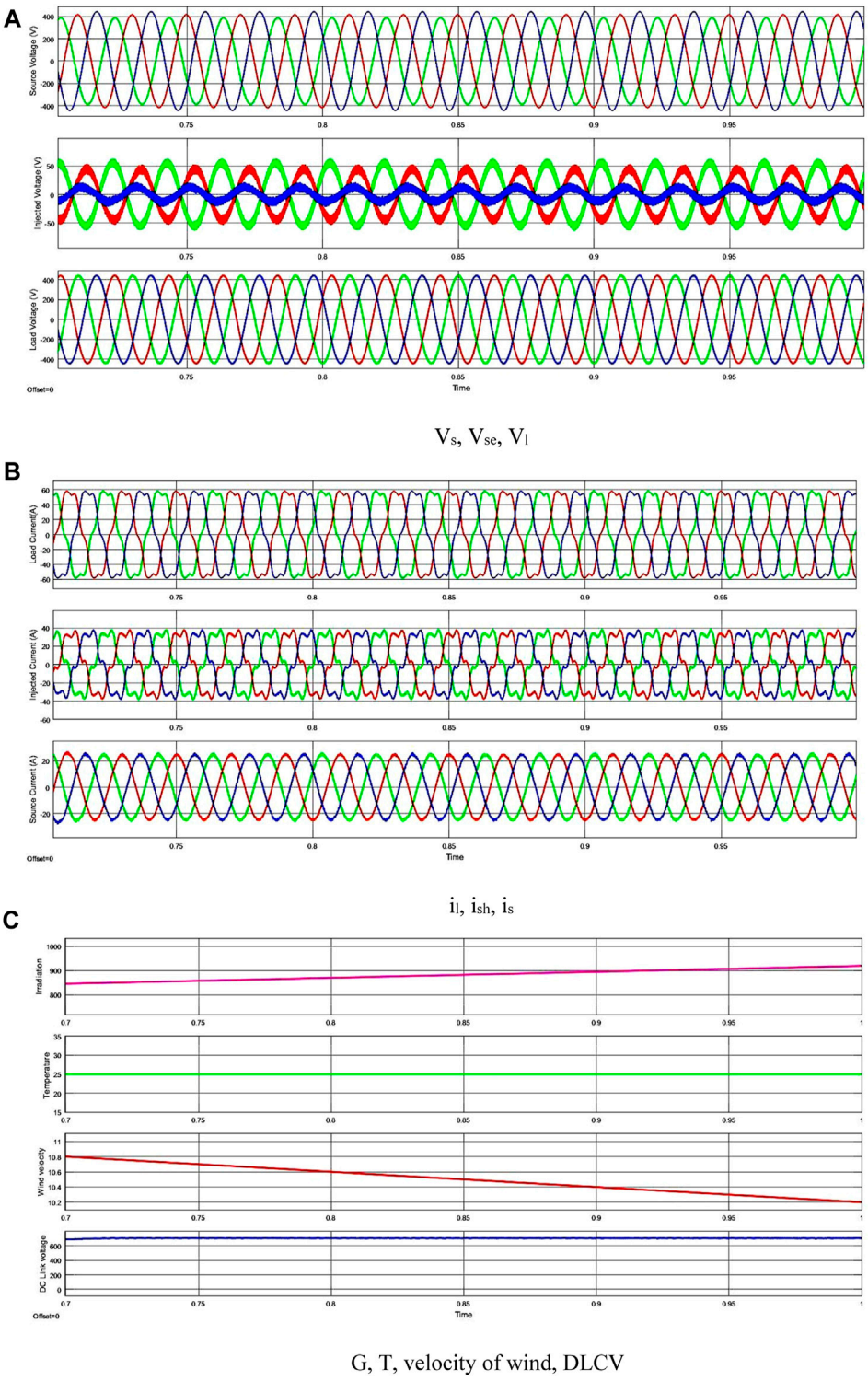

FIGURE 15
Waveforms for the third case study.

with the loads being taken into account. To demonstrate the improved performance of the designed system, Table 7 presents four different case studies with various combinations of non-linear loads and PQ issue conditions with variable wind velocity, solar irradiation, and so on. In this instance, the voltage source (VS) is chosen as an unequal phase supply for instances 3 and 4 and a balanced phase supply for studies 1 and 2. Cases 1 and 2 take into account the voltage sag, voltage swell, and voltage disturbance difficulties. Therefore, the goals were to minimize the THD, increase the PF, and maintain a constant DLCV. With the

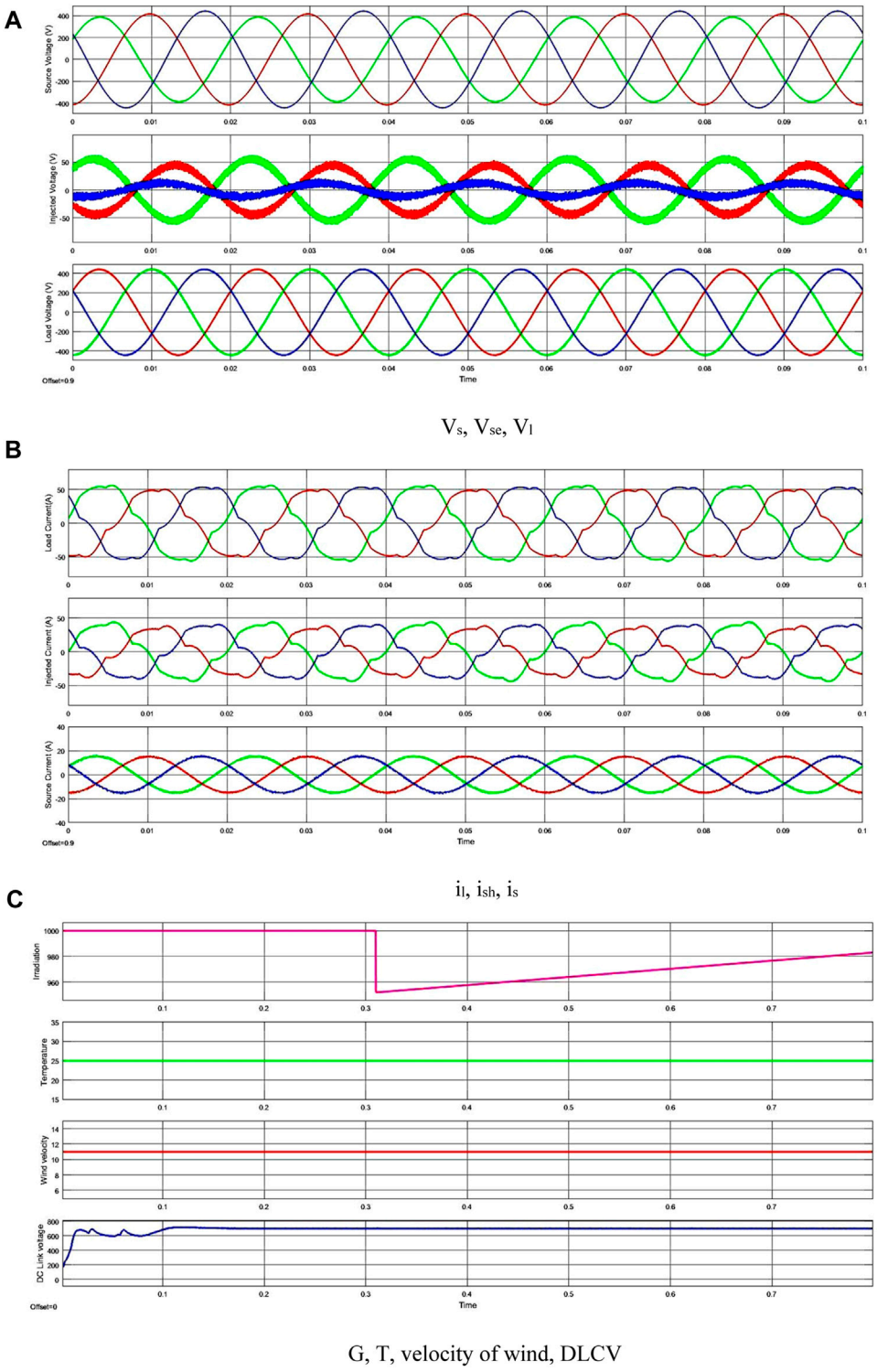

FIGURE 16
Waveforms of the suggested system for case 4.

purpose of demonstrating the effectiveness of the suggested ANFBC, synchronous reference frame theory (SRFT) comparison analysis was performed. Using Eq. 27, the PF is calculated from the THD.

$$THD = \frac{\left(\sqrt{I_2^2 + I_3^2 + ...I_n^2}\right)}{I_1}. \quad (27)$$

The voltage sag/swell ($V_{sag/swell}$) is evaluated by Eq. 28:

TABLE 8 THD and PF comparison.

Case	Method	THD	PF		
			Phase a	Phase b	Phase c
1	No UPQC	17.34	0.7764	0.7575	0.7752
	5L-UPQC with SRFT	3.74	0.9899	0.9845	0.9864
	5L-UPQC with pq	3.23	0.9866	0.9888	0.9841
	2L-UPQC with PM	3.48	0.9887	0.9878	0.9889
	3L-UPQC with PM	3.42	0.9877	0.9866	0.9974
	5L-UPQC with PM and GA	3.11	0.9997	0.9984	0.9995
	5L-UPQC with PM and ACO	3.01	0.9994	0.9991	0.9997
	5L-UPQC with PM and FBGO	**2.91**	**0.9989**	**1**	**1**
2	No UPQC	15.34	0.8664	0.8475	0.8652
	5L-UPQC with SRFT	3.88	0.9985	0.9988	0.9967
	5L-UPQC with pq	3.74	0.9867	0.9816	0.9822
	2L-UPQC with PM	3.86	0.9824	0.9865	0.9878
	3L-UPQC with PM	3.79	0.9924	0.9987	0.9991
	5L-UPQC with PM and GA	3.76	0.9996	0.9999	0.9998
	5L-UPQC with PM and ACO	3.64	0.9998	0.9999	1
	5L-UPQC with PM and FBGO	**3.63**	**1**	**0.9999**	**1**
3	No UPQC	27.90	0.8145	0.8998	0.7117
	5L-UPQC with SRFT	3.66	0.9988	0.9998	1
	5L-UPQC with pq	3.51	0.9845	0.9877	0.9855
	2L-UPQC with PM	3.62	0.9968	0.9979	0.9899
	3L-UPQC with PM	3.89	0.9888	0.9874	0.9854
	5L-UPQC with PM and GA	3.71	0.9997	1	0.9998
	5L-UPQC with PM and ACO	3.88	0.9995	0.9997	1
	5L-UPQC with PM and FBGO	**3.75**	**0.9999**	**1**	**0.9989**
4	No UPQC	19.86	0.6412	0.7012	0.7551
	5L-UPQC with SRFT	3.64	0.9981	0.9999	0.9985
	5L-UPQC with pq	3.78	0.9954	0.9955	1
	2L-UPQC with PM	3.78	0.9824	0.9821	0.9878
	3L-UPQC with PM	3.75	0.9997	0.9998	1
	5L-UPQC with PM and GA	3.78	1	0.9988	0.9998
	5L-UPQC with PM and ACO	3.68	1	0.9988	0.9998
	5L-UPQC with PM and FBGO	**3.50**	**1**	**0.9998**	**0.9998**

*PM, proposed ANN-based reference signal generation method.
The bold values shows the proposed method (to highlight the best result).

$$V_{sag/swell} = \frac{V_l - V_S}{V_l} = \frac{V_{se}}{V_l}. \quad (28)$$

The injected voltage by the series filter is calculated by Eq. 29:

$$V_{se} = V_l - V_S. \quad (29)$$

The injected current by the shunt filter is calculated by Eq. 30:

$$i_{sh} = i_i - i_S. \quad (30)$$

In case 1, the VS is initially considered to be balanced. To assess the performance of the SHAPF, a 30% balanced sag was

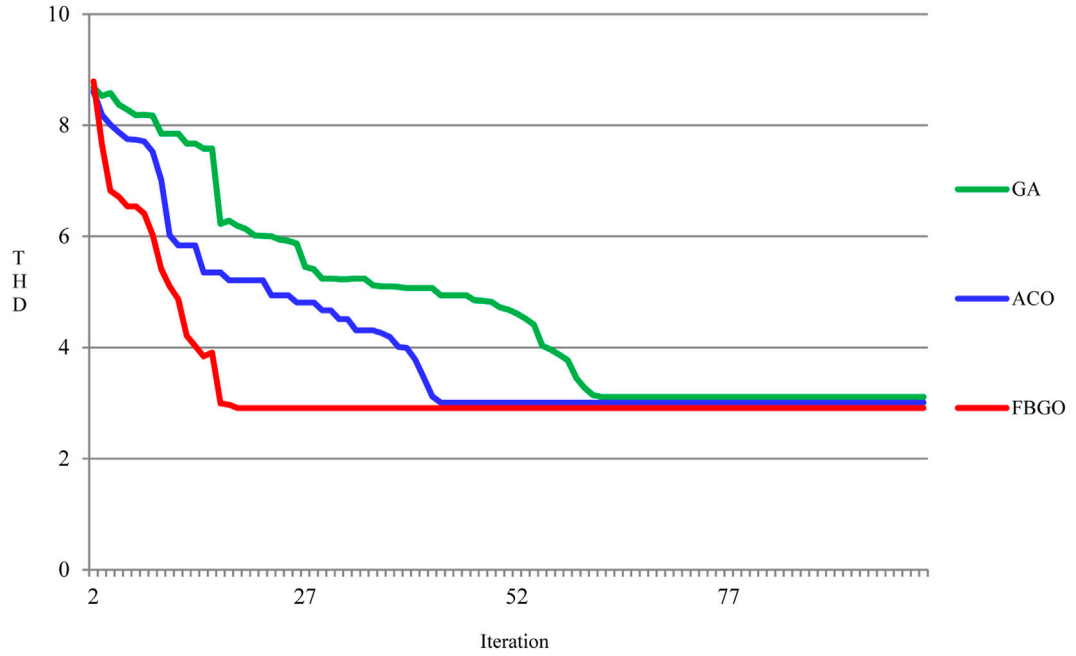

FIGURE 17
Case 1 convergence plot.

TABLE 9 Comparison of the design parameters.

Case	Method	R_{sh}	R_{se}	L_{sh}	L_{se}
1	5L-UPQC with PM and GA	0.01	1.45	1.32	5.2123
	5L-UPQC with PM and ACO	0.04	0.01	0.63	0.1581
	5L-UPQC with PM and FBGO	0.05	1.8	0.91	0.0321
2	5L-UPQC with PM and GA	0.21	0.21	3.45	3.0721
	5L-UPQC with PM and ACO	0.11	1.41	1.08	5.0464
	5L-UPQC with PM and FBGO	0.03	0.03	1.68	9.7308
3	5L-UPQC with PM and GA	0.37	1.61	4.29	2.0387
	5L-UPQC with PM and ACO	0.18	0.45	6.12	1.02
	5L-UPQC with PM and FBGO	0.08	1.72	0.32	3.24
4	5L-UPQC with PM and GA	0.37	1.01	9.21	4.1397
	5L-UPQC with PM and ACO	0.19	1.42	5.12	0.0132
	5L-UPQC with PM and FBGO	0.09	1.11	0.18	0.0736

intentionally introduced into the source voltage between the time interval of 0.25 and 0.35 s, as depicted in Figure 13A. However, the ANNC system effectively detects the voltage dip, applies a suitable compensating voltage through the coupling transformer, and maintains a consistent voltage at the load terminals. To further evaluate the performance of the SHAPF with the proposed ANFIS and FBGO optimally selected filter parameters, both loads 1 and 3 were considered simultaneously.

As shown in Figure 13B, the load current waveform exhibited contamination and non-sinusoidal behavior but remained balanced. The suggested approach mitigates the irregularities in the current waveform, leading to a reduction in the current's THD from 17.34% to 2.91% while concurrently raising the PF from 0.7764 to nearly unity. Furthermore, the proposed method sustains a steady DLCV for the load under the conditions of 11 m/s wind velocity, 1000 W/m^2 irradiation, and a constant temperature of 25°C, as represented in Figure 13C.

In case 2, similar to case 1, the source voltage is initially assumed to be balanced. To examine the working of the SHAPF under the conditions of a 30% swell and disturbance, these events are introduced during the time intervals of 0.4–0.5 s and 0.6–0.7 s, respectively. However, it is evident from Figure 14A that the ANNC effectively recognizes the voltage increase and disturbance, subsequently eliminating them by introducing the necessary compensating voltage.

The load current was found to be non-sinusoidal and unbalanced due to the presence of loads 2 and 4, as depicted in Figure 14B. Nevertheless, the proposed method manages to reduce the THD of the current from 15.34% to 3.63%, which is lower when compared to the SRFT and pq methods and raises the PF from 0.8664 to unity. It is important to note that the wind velocity and load fluctuations are considered simultaneously, with constant irradiation and temperature. However, the suggested approach maintains a steady DLCV of 700 V, as shown in Figure 14C.

In case 3, the source voltage is intentionally taken to be unbalanced, and the performance of the SHAPF is assessed under stable-state voltage conditions, as demonstrated in Figure 15A. Nevertheless, the ANNC effectively recognizes the inequalities in the phase voltage and rectifies it by inserting the necessary voltage. To examine the operation of the SHAPF, loads 1 and 2 are considered, resulting in the observation of a significantly contaminated yet balanced load current waveform, as seen in Figure 15B. The proposed system successfully rectifies the

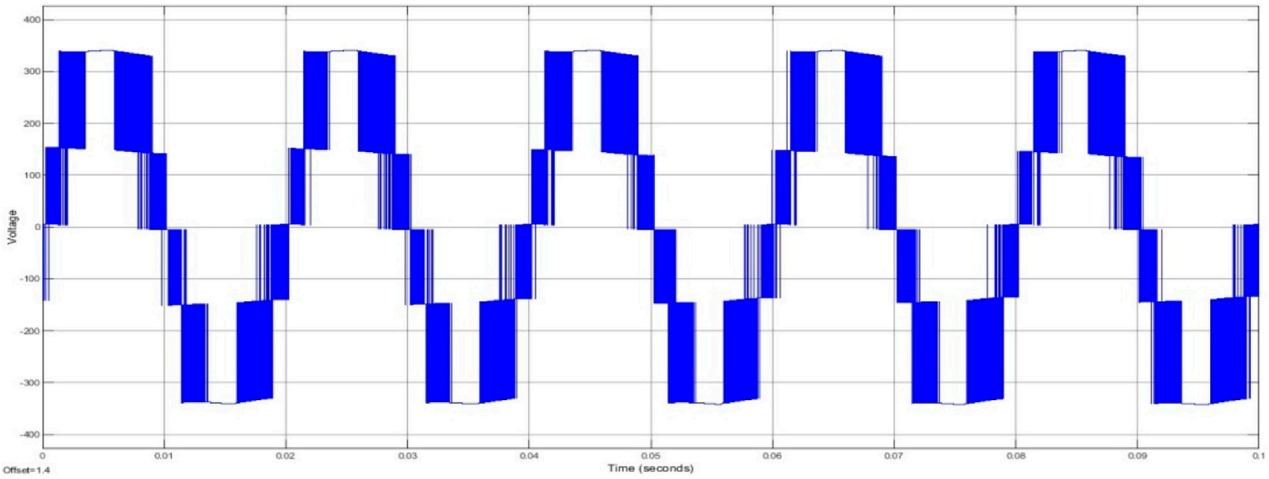

FIGURE 18
Switching voltage of 5L-UPQC.

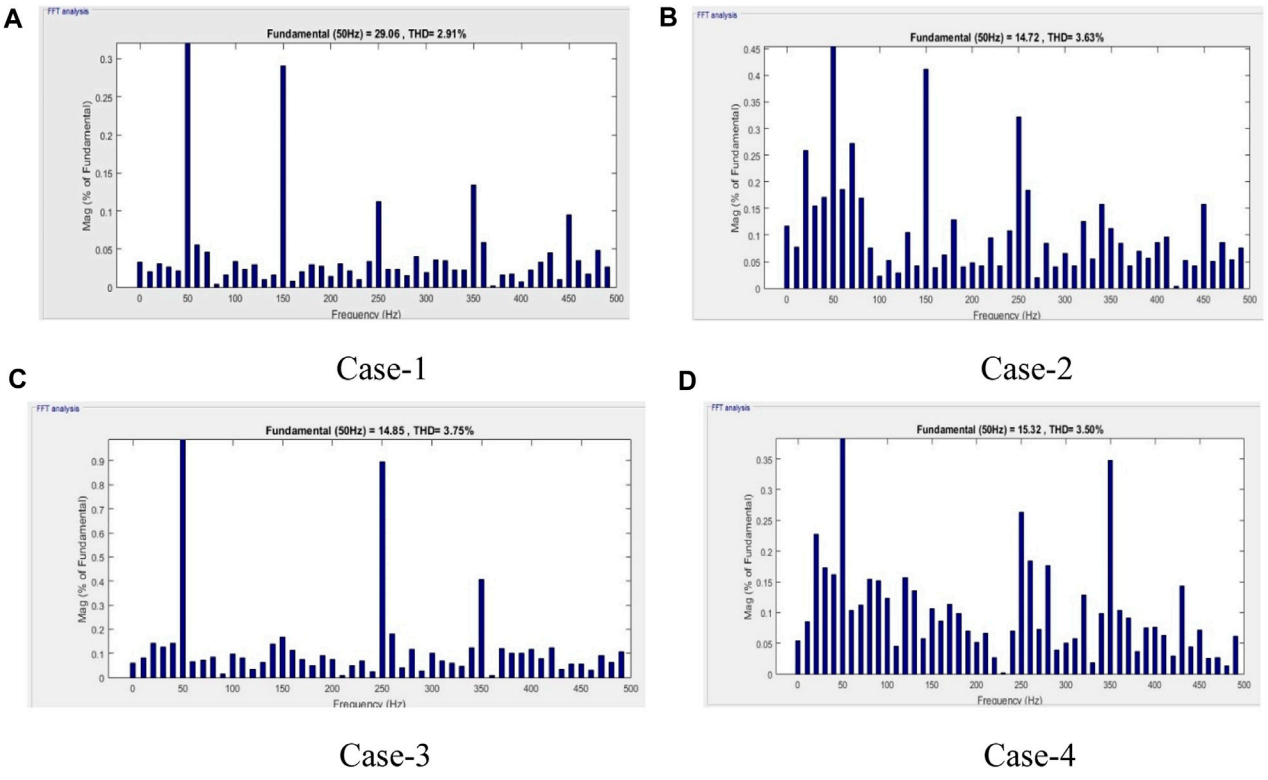

FIGURE 19
THD spectrum.

imperfections in the current waveform. The THD of the current is reduced from 27.90% to 3.75%, and the PF is elevated from 0.8145 to 0.9999. Furthermore, the suggested controller maintains a constant DLCV during variations in the load and solar irradiation, alongside a consistent wind velocity, as depicted in Figure 15C.

In case 4, the source voltage is intentionally set to be unbalanced, and the ANNC-controlled SHAPF adeptly identifies inequalities and successfully rectifies them, as depicted in Figure 16A. In this scenario, the simultaneous connection of loads 1 and 4 results in a contaminated and unbalanced load-current waveform, as illustrated in Figure 16B. However, the proposed SHAPF with FBGO functions efficiently, leading to a reduction in the THD of the current from 19.86% to 3.50% and a rise in the PF from 0.6412 to unity. Furthermore, the suggested controller successfully maintains

a consistent DLCV during load variations, as demonstrated in Figure 16C.

Table 8 provides a comparison of the THD and the PF between the proposed method and other techniques such as SRFT and pq theories with 5L and three levels of UPQC. Table 8 demonstrates that the proposed method significantly reduces the THD and boosts the PF in comparison to the other approaches. Figure 17 illustrates the convergence graph of the proposed FBGO in comparison to the genetic algorithm (GA) and ACO. This plot clearly demonstrates that the proposed FBGO achieves the lowest THD value in just 17 iterations, which is notably less when compared to the GA (62 iterations) and ACO (43 iterations). Moreover, Table 9 provides the optimized values of control variables. The output voltage of five-level UPQC is represented in Figure 18. Lastly, Figure 19 presents the FFT analysis of the current for the proposed system in the second case.

6 Conclusion

In this research, an approach based on ANNC is introduced for a 5L-UPQC interconnected with solar, wind, and battery sources. The ANN controller, trained with the Levenberg–Marquardt algorithm, is employed within the UPQC system to generate reference signals for the converters. This obviates the need for conventional transformations, like abc, dq0, and αβ. Furthermore, the optimization of filter parameters is achieved through football game optimization, and an ANFIS is proposed for the SHAPF to maintain a stable DLCV balance. The proposed 5L-UPQC system effectively sustains a constant DLCV, despite variations in loads, solar irradiation, and wind conditions. It successfully mitigates current harmonics, enhances the shape of the current waveform, resulting in an improved power factor, and effectively eliminates fluctuations in the grid voltage, such as interruptions, sags, swells, and disturbances. In the future, this approach can be extended to multilevel UPQC systems employing reduced switches.

Data availability statement

The raw data supporting the conclusion of this article will be made available by the authors, without undue reservation.

Author contributions

KS: conceptualization, investigation, methodology, and writing–original draft. GR: formal analysis, software, and writing–review and editing. PB: formal analysis, investigation, resources, software, supervision, and writing–review and editing. TS: funding acquisition, resources, visualization, and writing–review and editing.

Funding

The author(s) declare that no financial support was received for the research, authorship, and/or publication of this article.

Conflict of interest

The authors declare that the research was conducted in the absence of any commercial or financial relationships that could be construed as a potential conflict of interest.

Publisher's note

References

Belqasem, A., Rameshkumar, K., Vairavasundaram, I., and Ramachandran, S. (2022). A novel single-phase shunt active power filter with a cost function based model predictive current control technique. *Energies* 15, 4531. doi:10.3390/en15134531

Chandrasekaran, K., Selvaraj, J., Clement Raj Amaladoss, L. V., and Veerapan, L. (2021). Hybrid renewable energy based smart grid system for reactive power management and voltage profile enhancement using artificial neural network. *Energy Sources, Part A Recovery, Util. Environ. Eff.* 43 (No. 19), 2419–2442. doi:10.1080/15567036.2021.1902430

DheyaaIed, M., and Goksu, G. (2022). Design and control of three-phase power system with wind power using unified power quality conditioner. *Energies* 15, 7074. doi:10.3390/en15197074

Ganesan, A., and Srinath, S. (2019). Optimal controller for mitigation of harmonics in hybrid shunt active power filter connected distribution system: an EGOANN technique. *J. Renew. Sustain. Energy* 11. doi:10.1063/1.5085028

Hassan, K., Makdisie, C., IssamHoussamo, and Mohammed, N. (2022). New modulation technique in smart grid interfaced multilevel UPQC-PV controlled via fuzzy logic controller. *Electronics* 11, 919. doi:10.3390/electronics11060919

Imam, A. A., Kumar, R. S., and Yusuf, A. (2020). Modeling and simulation of a PI controlled shunt active power filter for power quality enhancement based on P-Q theory. *Electronics* 9, 637. doi:10.3390/electronics9040637

Khosravi, N., Abdolmohammadi, H. R., Bagheri, S., and Miveh, M. R. (2021). Improvement of harmonic conditions in the AC/DC microgrids with the presence of filter compensation modules. *Renew. Sustain. Energy Rev.* 143, 110898. doi:10.1016/j.rser.2021.110898

Khosravi, N., Echalih, S., Hekss, Z., Baghbanzadeh, R., Messaoudi, M., and Shahideipour, M. (2023). A new approach to enhance the operation of M-UPQC proportional-integral multiresonant controller based on the optimization methods for a stand-alone AC microgrid. *IEEE Trans. Power Electron.* 38 (3), 3765–3774. doi:10.1109/TPEL.2022.3217964

Koganti, S., Sujatha, C. N., Kumar Balachandran, P., Mihet-Popa, L., and Kumar, N. U. (2022). Optimal design of an artificial intelligence controller for solar-battery integrated UPQC in three phase distribution networks. *Sustainability* 14 (21), 13992. doi:10.3390/su142113992

KogantiKrishna, S. J. K., and Reddy Salkuti, S. (2022). Design of multi-objective-based artificial intelligence controller for wind/battery-connected shunt active power filter. *Algorithms* 15 (8), 256. doi:10.3390/a15080256

Lin, T.-C., and Simachew, B. (2022). Intelligent tuned hybrid power filter with fuzzy-PI control. *Energies* 15, 4371. doi:10.3390/en15124371

Mansoor, M. A., Hasan, K., Othman, M. M., Noor, S. Z. B. M., and Musirin, I. (2023). Construction and performance investigation of three phase solar PV and battery energy storage system integrated UPQC. *IEEE Accesses* 8, 103511–103538. doi:10.1109/ACCESS.2020.2997056

Marcel, N., Claudiu-Ionel, N., Dumitru, S., and Adrian, V. (2023). Comparative performance of UPQC control system based on PI-GWO, fractional order controllers, and reinforcement learning agent. *Electronics* 12, 494. doi:10.3390/electronics12030494

Mishra, A. K., Soumya, R. D., Prakash, K., Mohanty, A., and Mishra, D. K. (2020). PSO-GWO optimized fractional order PID based hybrid shunt active power filter for

power quality improvements. *IEEE Access* 8, 74497–74512. doi:10.1109/access.2020.2988611

Mishra, A. K., Soumya, R. D., Ray, P. K., Kumar Mallick, R., Mohanty, A., and Dillip, K. (2022). PS-O-GW-O optimized fractional order PID based hybrid shunt active power filter for power quality improvements. *IEEE Access* 8, 74497–74512. doi:10.1109/access.2020.2988611

NafehHeikalEl-Sehiemy, A. A. A. R. A., and Salem, W. A. A. (2022). Intelligent fuzzy-based controllers for voltage stability enhancement of AC-DC micro-grid with D-STATCOM. *D-STATCOM* 61 (3), 2260–2293. doi:10.1016/j.aej.2021.07.012

Okech, E. O., Zhang-Hui, L., Mali, X., Kamaraj, P., and Alukaka, J. R. (2022). Neural network controlled solar PV battery powered unified power quality conditioner for grid connected operation. *Energies* 15, 6825. doi:10.3390/en15186825

Pazhanimuthu, C., and Ramesh, S. (2018). Grid integration of renewable energy sources (RES) for power quality improvement using adaptive fuzzy logic controller based series hybrid active power filter (SHAPF). *J. Intelligent Fuzzy Syst.* 35, 749–766. doi:10.3233/jifs-171236

Rajesh, P., Shajin, F. H., and Umasankar, L. (2021). A novel control scheme for PV/wt/FC/battery to power quality enhancement in micro grid system: a hybrid technique. *Energy Sources, Part A Recovery, Util. Environ. Eff.* 1–17. doi:10.1080/15567036.2021.1943068

Ramadevi, A., Srilakshmi, K., Kumar, P., Colak, I., Dhanamjayulu, C., and Khan, B. 2023, Optimal design and performance investigation of artificial neural network controller for solar- and battery-connected unified power quality conditioner. *Int. J. Energy Res.* 2023, 1-22. doi:10.1155/2023/3355124

Renduchintala, U. K., Pang, C., Tatikonda, K. M., and Yang, L. (2021). ANFIS-Fuzzy logic based UPQC in interconnected microgrid distribution systems: modeling, simulation and implementation. *J. Eng.* 2021, 6–18. doi:10.1049/tje2.12005

Sahithullah, M., Kumar Ajithan, S., and Jayaraman, S. (2019). Optimal design of shunt active power filter for power quality enhancement using predator-prey based firefly optimization. *Swarm Evol. Comput.* 44, 522–533. doi:10.1016/j.swevo.2018.06.008

Sakthivel, A., Vijayakumar, P., SenthilkumarLakshminarasimman, A. L., and Paramasivam, S. (2015). Experimental investigations on ant colony optimized pi control algorithm for shunt active power filter to improve power quality. *Control Eng. Pract.* 42 (42), 153–169. doi:10.1016/j.conengprac.2015.04.013

Sarker, K., Chatterjee, D., and Goswami, S. K. (2020). A modified PV-wind-PEMFCS-based hybrid UPQC system with combined DVR/STATCOM operation by harmonic compensation. *Int. J. Model. Simul.* 41 (No.4), 243–255. doi:10.1080/02286203.2020.1727134

Sayed, J. A., Sabha, R. A., and Ranjan, K. J. (2021). Biogeography based optimization strategy for UPQC PI tuning on full order adaptive observer based control. *IET Generation, Transm. Distribution* 15, 279–293. doi:10.1049/gtd2.12020

Srilakshmi, K., Jyothi, K. K., Kalyani, G., and Sai Prakash Goud, Y. (2023). Design of UPQC with solar PV and battery storage systems for power quality improvement. *Cybern. Syst. Int. J.*, 1–30. doi:10.1080/01969722.2023.2175144

Srilakshmi, K., Srinivas, N., Balachandran, P. K., Reddy, J. G. P., Gaddameedhi, S., Valluri, N., et al. (2022). Design of soccer league optimization based hybrid controller for solar-battery integrated UPQC. *IEEE Access* 10, 107116–107136. doi:10.1109/access.2022.3211504

Sudheer, V., and Kota, V. R. (2017). Implementation of artificial neural network based controller for a five-level converter based UPQC. *Alexandria Eng. J.* 57 (Issue 3), 1475–1488. doi:10.1016/j.aej.2017.03.027

Szromba, A. (2020). The unified power quality conditioner control method based on the equivalent conductance signals of the compensated load. *Energies*, 13.

Yang, D., MaGaoMa, Z. X. Z., and Cui, E. (2019). Control strategy of intergrated photovoltaic-UPQC system for DC-bus voltage stability and voltage sags compensation. *Energies* 12, 4009. doi:10.3390/en12204009

Yap, H., MohdRadzi, M. A., Hassan, M. K., and Mailah, N. F. (2017). Control algorithms of shunt active power filter for harmonics mitigation: a review. *Energies* 10 (No.12), 2038. 2038. doi:10.3390/en10122038

Yap, H., MohdRadzi, M. A., Zainuri, M. A. A. M., and Md Zawawi, M. A. (2019). Shunt active power filter: a review on phase synchronization control techniques. *Electronics* 8, 791. doi:10.3390/electronics8070791

Zhao, X., Chai, X., Guo, X., Ahmad, W., Wang, X., and Zhang, C. (2021). Impedance matching-based power flow analysis for UPQC in three-phase four-wire systems. *Energies* 14, 2702. doi:10.3390/en14092702

Zhou, M., Wan, J.-Ru, Wei, Z.-Q., and Cui, J. (2006). "Control method for power quality compensation based on levenberg-marquardt optimized BP neural networks," in 2006 CES/IEEE 5th International Power Electronics and Motion Control Conference, Shanghai, China, August, 2006.

Nomenclature

5L-UPQC	**Five-level UPQC**
FBGO	Football game optimization
NCS	Non-conventional sources
PV	Photovoltaic
BSS	Battery storage system
PQ	Power quality
WPGS	Wind power generation system
ANN	Artificial neural network
UPQC	Unified power quality conditioner
LMBP	Levenberg–Marquardt backpropagation
ANFIS	Artificial neuro-fuzzy interface system
pq	Instantaneous reactive power
DLCV	Direct-current link capacitor voltage
SRFT	Synchronous reference frame theory
THD	Total harmonic distortion
PF	Power factor
GA	Genetic algorithm
PSO	Particle swarm optimization
PIC	Proportional integral controller
SHAPF	Shunt active power filter
GWO	Gray wolf optimization
PWM	Pulse-width modulation
BBC	Buck–boost converter
SMC	Sliding mode control
FLC	Fuzzy logic controller
VSC	Voltage source converter
MSE	Mean-square error
BBO	Biogeography-based optimization
SeAF	Series-active power filter
BC	Boost converter
ACO	Ant colony optimization
SCC	Short-circuit current
FOPID	Fractional-order proportional integral derivate
MSF	Membership function
FF-ANN	Firefly-based ANN
PPFFA	Predator–prey firefly algorithm
SPVGS	Solar photovoltaic power generation system
$\mathbf{V_{LL}}$	Line-to-line rms voltage
CE	Change in error
OL	Output layer of the ANN
IL	Input layer of the ANN
HL	Hidden layer of the ANN
E	Error
PEF	Performance function
PF	Power factor
HD	Hyper distance
CM	Coach's memory
L_{se}	SeAF inductance
V_{S_abc}	Source voltage for abc phases
V_m	Peak voltage of the system
$R_S L_S$	Grid resistance and inductance
m	Modulation index
V_{l_abc}	Load voltage for phases a, b, and c
C_{dc}	DC-link capacitance
V_{se_abc}	Voltage injected by the series filter in abc
$V_{se\_abc}^{ref}$	Reference compensated voltage in abc phases
i_{S_abc}	Source current for abc phases
i_{l_abc}	Load current for abc phases
R_{sh}	SHAPF resistance
$f_{sh} f_{se}$	Switching frequency
$V_{cr,pp}$	Peak-to-peak voltage ripple
V_{dc}	DC-link voltage
a_f	Overloading factor
V_{dc}^{ref}	Reference DLCV
i_{sh_abc}	Shunt filter compensated current in abc phases
Δi_{dc}	DC-link output error
$i_{sh\_abc}^{ref}$	Shunt filter reference compensated current in abc phases
i_{dc}^{ref}	Reference DC current
R_{se}	SeAF resistance
$V_{dc,err}$	DLCV error
$i_{BS,er}{}^{*}$	Reference battery error current
i_{ph}	Photocurrent source
i_{PV}	PV cell output current
L_{sh}	SHAPF inductance
i_d	Forward diode-carrying current
P_{dc}	DC-link power
$\mu_{Ai} \mu_{Bi}$	Membership functions of fuzzy
SOCOB	State of charge of the battery
$P^t{}_i$	$P^t{}_i$ indicates the ith position of the player
δ, γ	Random numbers
σ_i	Step size
Θ	Constant
$\mathbf{P^t{}_B}$	Position of the player containing the ball at the instant t